

# Towards Fine-Grained Indoor Localization based on Massive MIMO-OFDM System: Perspective of Multipath Components

Chenglong Li, Sibren De Bast, *Student Member, IEEE*, Emmeric Tanghe, *Member, IEEE*,  
Sofie Pollin, *Senior Member, IEEE* and Wout Joseph, *Senior Member, IEEE*

**Abstract**—Fine-grained indoor localization has attracted attention recently because of the rapidly growing demand for indoor location-based services (ILBS). Specifically, massive (large-scale) multiple-input and multiple-output (MIMO) systems have received increasing attention due to high angular resolution. This paper presents an indoor localization testbed based on a massive MIMO orthogonal frequency-division multiplexing (OFDM) system, which supports physical-layer channel measurements. Instead of exploiting channel state information (CSI) directly for localization, we focus on positioning from the perspective of multipath components (MPCs), which are extracted from the CSI through the space-alternating generalized expectation-maximization (SAGE) algorithm. On top of the available MPCs, we propose a generalized fingerprinting system based on different single-metric and hybrid-metric schemes. We evaluate the impact of varying antenna topologies, feeding metrics, sizes of the training set, and fingerprinting methods. The experimental results show that the proposed fingerprinting method can achieve centimeter-level positioning accuracy with a relatively small training set. Specifically, the distributed uniform linear array obtains the highest accuracy with about 1.63-2.5-cm mean absolute errors resulting from the high spatial resolution.

**Index Terms**—Massive multiple-input and multiple-output (MIMO), indoor localization, fingerprinting, multipath components, channel state information (CSI), orthogonal frequency-division multiplexing (OFDM), machine learning.

## I. INTRODUCTION

INDOOR location-based services (ILBS) have become an essential part of smart Internet-of-things (IoT) to support the extensive location-aware applications both in industry and social activities. Different from outdoor positioning, of which the precise location is usually provided by global navigation satellite systems (GNSS), numerous indoor localization solutions have been proposed based on different sensors and radio frequency (RF) platforms over the past decades. These include ultra-wideband (UWB), wireless fidelity (WiFi), radio frequency identification (RFID), Bluetooth, and multimodal-based systems, based on the requirement on accuracy, coverage and applicability [1]. Being available in most RF measurement devices, the received signal strength indicator (RSSI)

characterizes the attenuation of radio propagation and has been widely utilized for indoor localization. Although RSSI (model-based or fingerprinting-based) can achieve meter-level positioning accuracy, it suffers from unreliable performance due to the multipath effect and dynamic scenarios. Assisted by multiple antennas or frequencies, several commercial off-the-shelf (COTS) IoT devices can provide a relatively accurate estimation of angle-of-arrival (AoA) or time-of-flight (ToF). For instance, the UWB-based system [2] and WiFi-based systems [3]. Exploiting both angle-based (AoA) and distance-based (RSSI or ToF) metrics, [4], [5] have investigated the positioning accuracy of hybrid metrics and discussed the placement of RF devices based on the coverage requirement and positioning performance of the estimated metrics. Moreover, instead of utilizing geometric features (distance and angle), the received phase has also been used for accurate indoor localization due to its robustness to complex environment [6]–[8].

Unlike RSSI is the energy accumulation at the medium access control (MAC) layer, channel response as a physical (PHY) layer metric can characterize how RF signal propagates from the transmitter to the receiver. Precisely measuring the wireless channel generally involves dedicated setups, such as vector network analyzer (VNA) or software-defined radio (SDR), which challenge practical applications. But the advancement of RF hardware circuits results in an increasing number of COTS devices, such as Intel WiFi link 5300 NIC [9], [10], enabling channel response collection. Exploiting channel state information (CSI), some pioneer works have achieved sub-meter indoor positioning accuracy, even in cluttered scenarios [10]–[12]. In [3], a prototype SpotFi was established, which estimated the AoA via a two-dimensional (2-D) multiple signal classification (MUSIC) algorithm and localized the user based on the AoA from the direct path. In [13], similar to SpotFi, AoA and ToF were estimated from the calibrated CSI based on an improved MUSIC algorithm. Together with CSI amplitude-based fingerprints, an AoA-enhanced probabilistic fingerprinting method was established. Instead of estimating AoAs from CSI, [14], [15] proposed to utilize the CSI (amplitude or phase) directly to implement the fingerprinting system, which also achieved sub-meter median positioning accuracy.

Massive (or large-scale) multiple-input multiple-output (MIMO) systems do not only benefit communications in terms of channel capacity and spectral efficiency, but also have the potential for accurate localization due to the high angular

This work is supported in part by the Excellence of Science (EOS) project Multi-SERVICE Wireless NETWORKS (MUSE-WINET), by the Research Foundation Flanders (FWO) SB PhD fellowship under Grant 1SA1619N, and by the FWO project under Grant G098020N.

C. Li, E. Tanghe, and W. Joseph are with the WAVES group, Department of Information Technology, Ghent University-imec, 9052 Ghent, Belgium (e-mail: chenglong.li@ugent.be).

S. De Bast and S. Pollin are with the Department of Electrical Engineering, KU Leuven, 3000 Leuven, Belgium.

resolution. In [16], a closed-form estimating signal parameters via rotational invariance technique (ESPRIT) was proposed for the incoherently distributed sources. To address the positioning problem of the narrow-band massive MIMO system, especially in a multipath-rich scenario, [17] proposed to jointly process snapshots of several distributed arrays based on compressed sensing without line-of-sight (LoS) distinguishing, and achieve sub-meter accuracy with high probability. [18], [19] proposed the fingerprint-based localization for cellular massive MIMO systems based on machine learning. In [20], [21], massive MIMO channel sounder prototypes were built for indoor use cases. The CSI data was fed to deep convolutional neural networks (CNN) to train the positioning model and achieved sub-meter [20] and centimeter-level [21] accuracy, respectively. Moreover, instead of training from scratch, transfer learning was introduced in [21] to reduce the modeling time, which relieved CNN's dependence on the scenario variety to some extent, and made CNN-based solution more practical.

In this paper, we focus on the fine-grained indoor localization based on a massive MIMO system, and propose to localize the user through the multipath components (MPCs). The main contributions of this paper are as follows.

- 1) We have established a massive MIMO indoor localization testbed, which supports PHY-layer metric collection, namely, channel state information. Different antenna topologies, including uniform linear array (ULA), distributed ULA (DIS), and uniform rectangular array (URA), have been investigated.
- 2) We have calibrated the CSI offsets across frequency and antenna domain due to synchronization and hardware errors. On top of that, the MPCs have been extracted and analyzed based on the space-alternating generalized expectation-maximization (SAGE) algorithm.
- 3) We have implemented a fingerprinting system based on the extracted MPCs. Different single-metric and hybrid-metric schemes have been investigated. The corresponding positioning performance has been evaluated and analyzed through the proposed classification and regression models from the perspective of MPCs.
- 4) The proposed MPCs-based fingerprinting method is generalized from the perspective of propagation. It requires less training set than the existing deep learning-based massive MIMO indoor positioning solutions (e.g., CNN-based method [21]).

The remainder of this paper is organized as follows. Section II introduces the system setting of the massive MIMO campaign and details of the CSI collection. Moreover, the CSI calibration is also discussed in this section. In Section III, the MPCs extraction based on the calibrated CSI is presented. Exploiting the extracted MPCs, the regression- and classification-based fingerprinting systems are established. In Section IV, the positioning performance is evaluated and analyzed. Furthermore, potential future directions are discussed. Finally, Section V concludes this paper.

*Notation:* Vectors and matrices are denoted by lower case boldface letter  $\mathbf{a}$  and upper case boldface letter  $\mathbf{A}$ , respectively. The set of  $M \times N$  real and complex matrices are denoted by

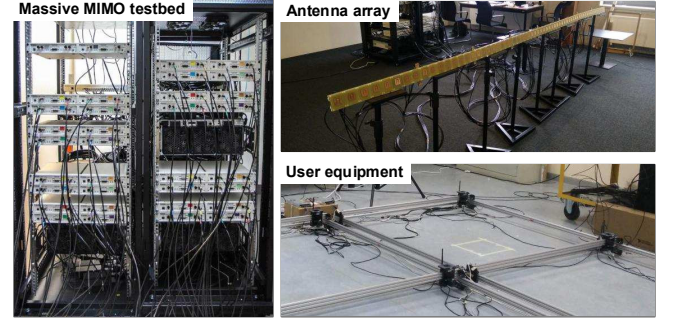


Fig. 1. Measurement setups: massive MIMO testbed, antenna array and user equipment.

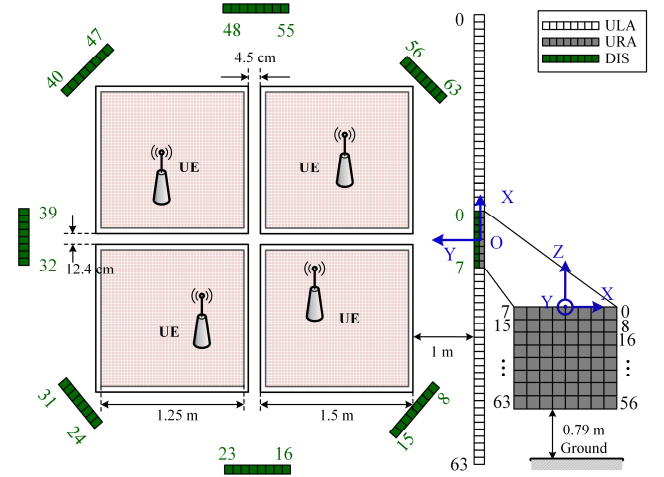


Fig. 2. Massive MIMO measurement campaign of CSI collection. Different antenna topologies are included: uniform linear array (ULA), distributed ULA (DIS), and uniform rectangular array (URA). UE represents the user equipment.

$\mathbb{R}^{M \times N}$  and  $\mathbb{C}^{M \times N}$ , respectively.  $j = \sqrt{-1}$  is the imaginary unit.  $(\cdot)^T$  represents the transpose operator,  $(\cdot)^H$  the conjugate transpose operator.  $\odot$  denotes the Hadamard product operator.  $|\cdot|$  and  $\|\cdot\|$  denote the absolute value and  $l_2$ -norm operator, respectively.  $\text{mode}(\cdot)$  is the most frequent value finding operator. Further,  $\mathcal{F}_N^{-1}(\cdot)$  represent the  $N$ -point discrete inverse Fourier transform.

## II. MASSIVE MIMO EXPERIMENT

### A. Channel State Information Collection

Based on the massive MIMO testbed at KU Leuven ESAT-TELEMIC [21], [22], the single-cell channel response is collected under different kinds of antenna topologies. The involved massive MIMO system consists of a base station (BS), equipped with 64 antennas, and the four universal software radio peripherals (USRPs) with a single dipole antenna each, acted as the user equipment (UE), as shown in Fig. 1. During the measurement, the BS is under the control of LabVIEW Communications MIMO Application Framework [23], which allows performing CSI measurement between the BS and the UE. In this massive MIMO system, a time division duplex-based frame structure has been adopted. The

BS (all 64 antennas) receives the orthogonal pilots sent by the four UEs simultaneously and conducts the channel estimation. The pilot tone consists of 100 sub-carriers, which are evenly spaced in frequency. Therefore, the measured CSI of a single transmission can be represented by the complex matrix,

$$\mathbf{H}_{\text{CSI}} = \{H_{n_r, n_k}\} \in \mathbb{C}^{64 \times 100}, \quad (1)$$

where  $n_r \in \{1, 2, \dots, 64\}$ ,  $n_k \in \{1, 2, \dots, 100\}$  represent the index of antenna and sub-carrier, respectively. The center frequency of the massive MIMO system is 2.61 GHz and bandwidth 20 MHz. The transmitted power is 15 dBm.

The massive MIMO testbed has been designed for the flexible deployment of the antenna arrays. It provides three topologies of the antenna array for CSI collection, specifically, a uniform linear array (ULA) of  $1 \times 64$  antennas, a uniform rectangular array (URA) of  $8 \times 8$  antennas, and eight distributed ULAs of  $1 \times 8$  antennas (DIS). The spacing between the adjacent antenna elements is 7 cm. The height of both ULA and DIS is one meter, while the lowest antenna elements of URA are located 79 cm above the floor. To collect the CSI from different UEs, four dipole-antenna USRPs are deployed within a targeted area  $3\text{m} \times 3\text{m}$ . The height of UE is 40 cm. Fig. 2 shows the measurement campaign and antenna arrays' deployment. The UEs are moved by the computerized numerical control (CNC) X-Y table along a zigzagged trajectory, which guarantees the collected ground truth of UE with less than 1-mm error. The moving stride of UE is 5 mm, so we have collected 252004 CSI samples in total for the four UEs. The dataset is publicly available [24] to encourage further research.

### B. Channel State Information Calibration

As a fine-grained PHY layer metric, CSI depicts the rich channel characteristics via the acute phase reacting in time, frequency (multi-frequency), and space (multi-antenna) domain. However, when conducting channel estimation under the assumption of perfect time and frequency synchronization between the transceiver, the actual phase in the measured CSI will be contaminated by the synchronization errors. To this end, the received phases suffer from the sampling frequency offset (SFO), and symbol timing offsets (STO), etc. [25], [26]. According to [27], [28], the implementation of orthogonal frequency division multiplexing (OFDM)-based PHY layer is susceptible to the effect of in-phase and quadrature-phase (IQ) imbalance in the front-end analog processing, which may cause nonlinear phase distortion on CSI. Due to the random initial phase generated by the local voltage controlled oscillator and imperfect compensation of the phase-locked loop, carrier phase offsets (CPO) are imposed on the received phases. Moreover, it should be noted that even though we have adopted the same type of antenna and equally long cables, there are possible phase offsets across antennas due to the heterogeneity of hardware. We did not calibrate across the antenna elements before the CSI measurement.

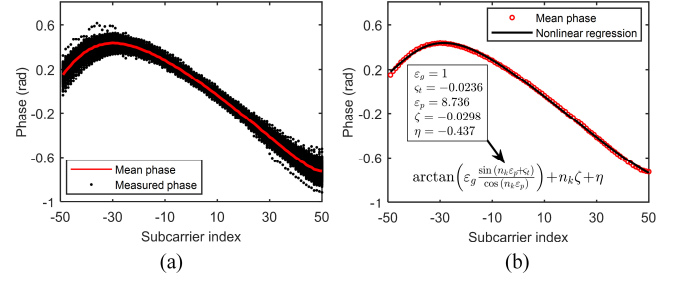


Fig. 3. (a) Residual phase offsets of 500 CSI samples after removing the LoS channel response, and the corresponding mean residual phase. (b) Nonlinear fitting results on the mean residual phase.

Overall, the measured CSI in the presence of the aforementioned phase errors can be given by,

$$\tilde{H}_{n_r, n_k} = \left( \sum_{l=1}^L H_{n_r, n_k}^{(l)} \right) \cdot \exp\left(-j\left(\zeta_{\text{SFO}}^{(n_k)} + \zeta_{\text{STO}}^{(n_k)} + \zeta_{\text{IQ}}^{(n_k)}\right)\right) \cdot \exp\left(-j\left(\eta_{\text{CPO}} + \varepsilon_{\text{ant}}^{(n_r)}\right)\right) + \omega, \quad (2)$$

where the first item on the right side is the desired multipath channel response.  $L$  is the number of propagation paths, and  $\omega$  the complex noise in the CSI matrix.  $\zeta_{\text{SFO}}$ ,  $\zeta_{\text{STO}}$ , and  $\zeta_{\text{IQ}}$  represent the phase shift caused by SFO, STO, and IQ imbalance, respectively. The SFO phase shift is proportional to the subcarrier index, which can be mitigated through a multiple linear regression across subcarriers [3], [26]. Due to the cyclic-shifting of channel impulse response (CIR), STO results in the high amplitude peaks at the far end of the power delay profile (PDP) [26], which can be utilized to calibrate the STO. So the most frequent far-end peak index among multiple packets can be obtained by,

$$\hat{K}_{\text{STO}} = \text{mode} \left( \arg \max_{n_k} |\mathcal{F}_{100}^{-1}(H_{n_k})|^2 \right), n_k > 1, \quad (3)$$

where  $n_k > 1$  means that the first peak of the PDP generally is the LoS link. So the estimated STO can be expressed as  $\zeta_{\text{STO}}^{(n_k)} = \frac{n_k \hat{K}_{\text{STO}}}{100}$  [26], where 100 is the number of subcarriers. But we can observe that for a specific  $\hat{K}_{\text{STO}}$ ,  $\zeta_{\text{STO}}$  also presents a linear relationship with the subcarrier index. To this end, we also can utilize linear regression to estimate the STO.

According to the experimental results in [28], the nonlinear phase shift caused by IQ imbalance is quite stable along the time scale but sensitive to the frequency. Fig. 3(a) presents 500 samples of the residual measured phase after removing the LoS channel response based on the ground truth. It can be observed that the phase shifts caused by IQ imbalance for different samples present a similar tendency along the subcarrier index, which means the sampling location has little impact on the calculation of IQ imbalance. To this end, we can calibrate the IQ imbalance by a nonlinear fitting on

$$\zeta_{\text{IQ}}^{(n_k)} = \arctan \left( \varepsilon_g \frac{\sin(n_k \zeta_t + \varepsilon_p)}{\cos(n_k \zeta_t)} \right), \quad (4)$$

where  $\varepsilon_g$ ,  $\varepsilon_p$  represent the gain and phase mismatch, respectively.  $\zeta_t$  denotes the unknown time offset.

The phase offset caused by CPO is represented by  $\eta_{\text{CPO}}$  in (2), which can be regarded as a random constant after the initiation of the transceiver [13]. In summary, we can calibrate the phase shifts caused by SFO, STO, CPO, and IQ imbalance through the following nonlinear regression,

$$\arg \min_{\Upsilon} \sum_{n_k} \left( \Delta \bar{\Theta}_{n_k} - \zeta_{\text{IQ}}^{(n_k)} - n_k \zeta_{\text{SFO/STO}} - \eta_{\text{CPO}} \right)^2, \quad (5)$$

where  $\Upsilon = [\varepsilon_g, \zeta_t, \varepsilon_p, \zeta_{\text{SFO/STO}}, \eta_{\text{CPO}}]$ .  $\Delta \bar{\Theta}$  denotes the average residual phase offset after removing the LoS channel response based on the ground truth of transceiver. The regression problem (5) can be solved via the Levenberg–Marquardt algorithm. Fig. 3(b) shows the nonlinear fitting results and the involved parameters for the CSI calibration.

Moreover, as mentioned above, even though we utilized the same type of antenna and the same length of cables, there still exists phase offsets due to the heterogeneity of hardware components. As presented in (2),  $\xi_{\text{ant}}$  is constant along the frequency and time scale, but variant across antenna elements. Since the BS (all the receiver antennas) shares the same oscillator and local reference time, it is reasonable to presume that all the phase shifts, except for  $\xi_{\text{ant}}^{(n_r)}$ ,  $n_r \in (1, 2, \dots, 64)$ , are constant along the antenna domain. It should be noted that the reported phases from the CSI are wrapped between  $-\pi$  to  $\pi$ . To avoid the phase ambiguity towards the estimation of  $\xi_{\text{ant}}^{(n_r)} \in (-\pi, \pi]$ , we estimate the antenna phase shift in the complex field, given by,

$$\arg \min_{\xi_{\text{ant}}^{(n_r)}} \left| \sum_{n_{\text{RP}}} \sum_{n_k} \left( \exp(j\Delta\Psi_{n_k, n_{\text{RP}}}) - \exp(j\xi_{\text{ant}}^{(n_r)}) \right) \right|^2, \quad (6)$$

where  $\Delta\Psi$  is the residual phase after the nonlinear calibration mentioned above.  $n_{\text{RPs}}$  is the index of the reference points (RPs) for calibration. We can select a small part of the CSI dataset acting as RPs to mitigate the nonlinear phase shifts and antenna phase offsets. Notably, for the fingerprinting system (will be introduced in Section III-B), the RPs for calibration are self-contained (i.e., the grids of fingerprints).

### III. FINGERPRINTING SYSTEM: PERSPECTIVE OF MPCs

#### A. MPCs Extraction

Different from the CSI depicting the channel between transceivers implicitly, the MPCs characterize the propagation from the perspective of power and geometry (angle and distance), which makes the channel model more explainable. Under assumption of a far-field and time-invariant MIMO channel, the channel transfer function at the  $k$ -th frequency bin  $f_k$ , ( $1 \leq k \leq K$ ) is given by

$$\mathbf{H}(f_k) = \sum_{l=1}^L \alpha_l c_{\text{Rx}}(\boldsymbol{\Omega}_{\text{Rx}, l}) c_{\text{Tx}}^\top(\boldsymbol{\Omega}_{\text{Tx}, l}) \exp(-j2\pi f_k \tau_l), \quad (7)$$

where  $\alpha_l, \tau_l$  denote the amplitude, and time of flight (ToF) of the  $l$ -th multipath, respectively.  $c_i(\boldsymbol{\Omega}_{i, l})$ , ( $i = \text{Tx}, \text{Rx}$ ) is the steering vector at transceiver. The directional vector  $\boldsymbol{\Omega}_{i, l}$  is uniquely determined by the spherical coordinates  $(\theta_{i, l}, \varphi_{i, l}) \in [-\frac{\pi}{2}, \frac{\pi}{2}] \times [0, \pi]$ , namely,  $\boldsymbol{\Omega}_{i, l} =$

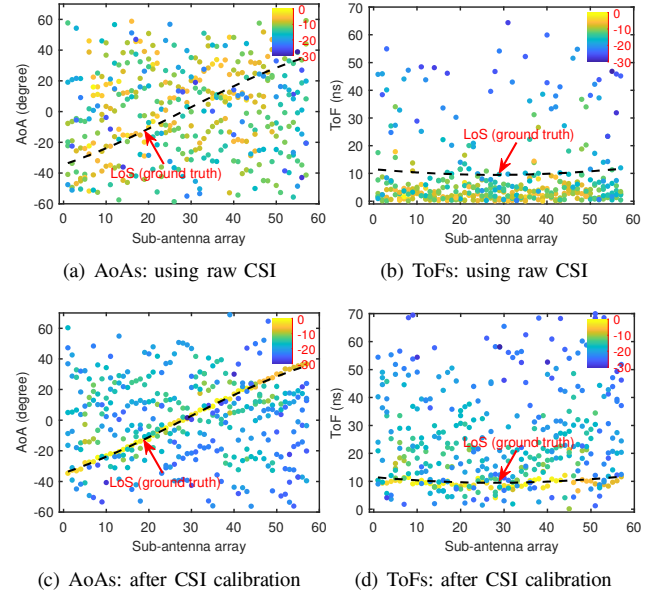


Fig. 4. Multipath components of ULA using the 8-element sliding sub-antenna arrays. The colorbar denotes the normalized power of each multipath component in dB.

$[\sin \theta_{i, l} \cos \varphi_{i, l}, \sin \theta_{i, l} \sin \varphi_{i, l}, \cos \theta_{i, l}]^\top$ , where  $\theta_{i, l}, \varphi_{i, l}$  represent the elevation angle of arrival (E AoA), azimuth angle of arrival (A AoA), respectively. In this paper, we only consider the angle at the receiver side because the UE's antenna is a single dipole. To extract the specular MPCs  $\Theta = [\alpha_l, \theta_l, \varphi_l, \tau_l]$  from the CSI, we introduce a computationally efficient frequency domain (FD) SAGE algorithm, which updates channel parameters sequentially with low-dimensional maximization steps. In [29], the serial interference cancellation with FD-SAGE was proposed for stable performance in multipath-rich scenarios. The expectation step (E-step) is given as

$$\hat{Y}_l(k; \hat{\Theta}') = \mathbf{H}(f_k) - \sum_{l'=1}^{l-1} \mathbf{S}(f_k; \hat{\Theta}_{l'}) \quad (8)$$

where  $\hat{\Theta}'$  is the parameter estimated in the last iteration.  $\mathbf{S}(f_k; \Theta_l) = \alpha_l c_{\text{Rx}}(\boldsymbol{\Omega}_{\text{Rx}, l}) \exp(-j2\pi f_k \tau_l)$ . Then, the maximization steps (M-step) of coordinate-wise updating can be given as follows,

$$\hat{\tau}_l'' = \arg \max_{\tau_l} \left\{ \left| z(\tau_l, \hat{\theta}_l', \hat{\varphi}_l'; \hat{Y}_l(k; \hat{\Theta}')) \right|^2 \right\}, \quad (9)$$

$$\hat{\theta}_l'' = \arg \max_{\theta_l} \left\{ \left| z(\tau_l'', \theta_l, \hat{\varphi}_l'; \hat{Y}_l(k; \hat{\Theta}')) \right|^2 \right\}, \quad (10)$$

$$\hat{\varphi}_l'' = \arg \max_{\varphi_l} \left\{ \left| z(\tau_l'', \hat{\theta}_l'', \varphi_l; \hat{Y}_l(k; \hat{\Theta}')) \right|^2 \right\}, \quad (11)$$

$$\hat{\alpha}_l'' = \frac{1}{MK} \cdot z(\tau_l'', \hat{\theta}_l'', \hat{\varphi}_l''; \hat{Y}_l(k; \hat{\Theta}')), \quad (12)$$

where  $M$  is the number of antennas at BS, and

$$z(\tau_l, \theta_l, \varphi_l; Y_l) = c^H(\theta_l, \varphi_l) \sum_{k=1}^K \exp(j2\pi \tau_l f_k) \odot Y_l(k). \quad (13)$$



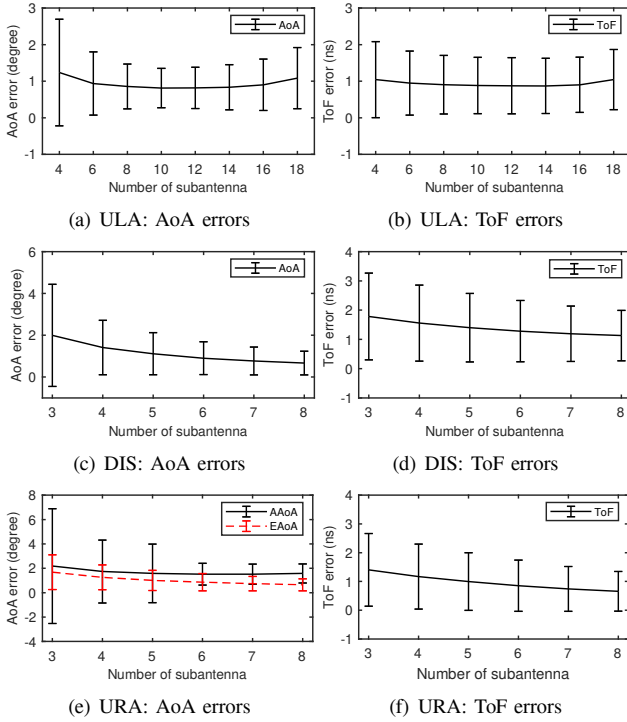


Fig. 5. Impact of antenna number in sub-array: the mean estimation accuracy of AoA and ToF with standard deviations.

The iterations stop when the power of a single path is 30 dB below the peak path power. In this way, we can determine the number of paths  $L$  as well. Besides E-step and M-step above, the initialization of  $\Theta$  is also related with algorithm performance and convergence. According to [29], [30], ToF and AoA can be initialized through frequency/spatial correlation, or beamforming, etc. Moreover, for the ULA, there is no information about elevation. So for the ULA and DIS topologies in our experiment, only azimuth is available. In this case, the  $c_{\text{Rx}}(\Omega_{\text{Rx},l})$  in (7) can be simplified as  $c_{\text{Rx}}(\varphi_l) = \{\exp(-j\frac{2\pi d}{\lambda}(m-1)\sin\varphi_l)\} \in \mathbb{C}^{M \times 1}$ ,  $m = 1, 2, \dots, M$ , where  $d$  is the spacing between the adjacent antenna, and  $\lambda$  the wavelength. The M-step for ULA should also be modified correspondingly. We refer to [29] for the detailed algorithm.

As the prerequisite of (7) presented, FD-SAGE algorithm in (8)-(13) is under the far-field assumption, which generally requires the distance between the transceiver, or the distance from scatterer to the transceiver is smaller than the Rayleigh distance, defined by  $2D^2/\lambda$ , where  $D$  is the largest dimension of the antenna array. Therefore, the Rayleigh distance for the ULA ( $1 \times 64$ ), DIS ( $1 \times 8$ ), and URA ( $8 \times 8$ ) in our experiment are 349.35 m, 5.46 m, and 9.25 m, respectively, which may be not easy to satisfy for indoor scenarios (especially for ULA). To apply the FD-SAGE algorithm here, the large antenna array is divided into multiple successive sub-arrays by a sliding window. Fig. 4 presents the MPCs results of the ULA without or with CSI calibration using the 8-element sliding sub-array. It can be observed that there are clear LoS-trajectories of AoA and ToF along the sub-antenna arrays after the calibration. The LoS components are distinguished clearly by the higher path power. Moreover, in Fig. 4(c), the AoAs of the LoS

path present distinct angle offsets along the antenna array, which verifies the spherical wavefront phenomenon of the large antenna array.

Instead of using the Rayleigh distance to determine the size of the sub-array, we specify the size by evaluating the estimated MPCs' accuracy in the case of different numbers of the antenna elements. Fig. 5 presents the mean absolute errors (MAEs) of AoA and ToF of LoS link, as well as the standard deviations (STDev). Due to the limited bandwidth (20 MHz), we identify the LoS path by pinpointing the components with the highest power instead of the shortest delay in the wideband system. Figs. 5(a) and (b) show that for the long ULA topology, the accuracy of either AoA or ToF decreases if the number of the antenna elements is too small or too large. When the number of antennas is between 8 and 14, the estimating accuracy is relatively stable (about 0.86-degree MAEs with 0.61-degree STDev, and 0.89-ns MAEs with 0.77-ns STDev). Therefore, the ULA sub-array size is selected as  $1 \times 8$  for later positioning evaluation, namely the multiple sub-arrays given as  $1 \times 8 \times 57$ . In Figs. 5(c) and (d), the estimation errors decrease as increasing the number of antenna elements in the sub-array for the DIS topology. When the number of antennas is 8, the MAEs of AoA and ToF achieve about 0.66 degree and 1.13 ns, respectively. So we have not partitioned the distributed ULA further and kept the multiple sub-arrays as  $1 \times 8 \times 8$ . When it comes to the URA, as presented in Figs. 5(e) and (f), the ToF prefers a larger number of antennas in the sub-array to increase accuracy, whereas the estimated errors of AoA (azimuth and elevation) become steady (1.51-degree MAEs for azimuth and 0.86-degree MAEs for elevation) when the number of antennas equals six. When converting the AoA's and ToF's errors into spatial errors (or based on the analysis in Section III-B.2), it is reasonable to take the AoA accuracy as the benchmark. Therefore, we set sub-array size as  $6 \times 6$ , namely the multiple sub-arrays as  $6 \times 6 \times 9$ , to guarantee more partitions and increase the spatial resolution of the URA.

### B. Fingerprinting System

Fingerprinting-based positioning techniques localize the UE by comparing its location-related metric(s) to a predefined radio map on the targeted area. In this paper, we propose to utilize the MPCs extracted from the CSI to form the fingerprinting metrics. Note that the measurement campaign was conducted in an LoS-dominated scenario as presented in Fig. 2. Therefore, only the MPCs from the direct links have been used for the fingerprinting system. In Fig. 6, during off-line phase, a grid of CSIs at the RPs is collected, and calibrated using (5) and (6) in Section III-A. The involved parameters for CSI calibration are stored at the local database (radio map) for later online processing directly. The MPCs, including amplitude, AoA, and ToF of each path, are extracted based on FD-SAGE. For fingerprint matching, there are generally two mapping solutions: classification and regression. For the classification scheme, the MPCs of all RPs are stored in the radio map, whereas only the trained matching model for the regression scheme. When localizing the UE (online phase), the parameters stored in the database is exploited for the

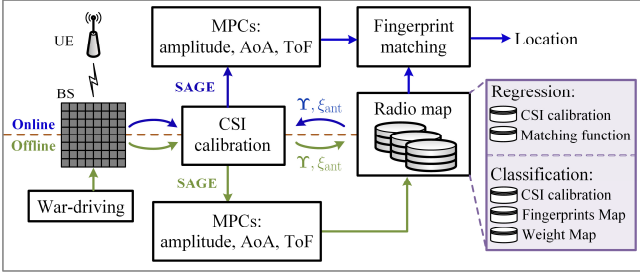


Fig. 6. The overall fingerprinting system architecture.

new coming CSI calibration. The UE's location is determined through the fingerprint mapping between the online MPCs and the radio map. This section will focus on designing the radio map and matching algorithms in both regression and classification schemes.

1) *Regression Scheme*: In the framework of regression, the objective is to find a nonlinear mapping between the input metrics  $\mathcal{X}$  and the UE's coordinates  $\mathcal{Y}$ , namely  $\mathcal{M} : \mathcal{X} \in \mathbb{R}^D \rightarrow \mathcal{Y} \in \mathbb{R}^2$  (2-D positioning), where  $D$  is the number of the input features. The metric can be the amplitude, AoA, and ToF of MPCs. In this paper, we introduce  $\epsilon$ -support vector regression ( $\epsilon$ -SVR) [31] to conduct the nonlinear mapping, which allows at most  $\epsilon$  deviation from the actual targets. To manage nonlinear regression, the kernels, such as the Gaussian kernel, have been utilized to map the input metric to higher dimensional feature space and then apply the standard  $\epsilon$ -SVR algorithm. It should be noted that only one output target is available for the regression in  $\epsilon$ -SVR, so we implement two SVR models for the 2-D positioning ( $x$  and  $y$  separately). The parameters involved in SVR, including the  $\epsilon$ -insensitive band, kernel scale, and regularization term strength, are optimized though the Bayesian optimization automatically. Besides a single metric (amplitude, AoA, or ToF), we also consider the hybrid schemes of these three metrics, as well as the two-metric combinations. These hybrid metrics can be fed to the nonlinear SVR model directly, which will be assigned different weights at a higher dimensional feature space.

2) *Classification Scheme*: Concerning classification, the UE position is estimated by finding the nearest one (or several) RP(s) based on the trained classifier. In this paper, a widely adopted light-weight classifier in the fingerprinting system, weighted  $k$ -nearest neighbour (w-kNN), has been introduced for the classification-scheme positioning, where the weights are the inverse of metrics distances (e.g.,  $l_2$  norm). Furthermore, we also consider the single- and hybrid-metric based solutions regarding different combinations of MPCs. For the single-metric scheme, the features are matched directly via w-kNN, which pinpoints the  $k$  nearest RPs as the estimation. However, for the hybrid-metric scheme, it is not recommended to simply fed the combined features to the w-kNN due to the different scale, reliability, and positioning accuracy of each MPC. Moreover, the MPCs from each sub-array is highly related, especially for ULA and URA. It is not reasonable to assume the conditional likelihood of the estimated metrics from each sub-array are independent and identically distributed

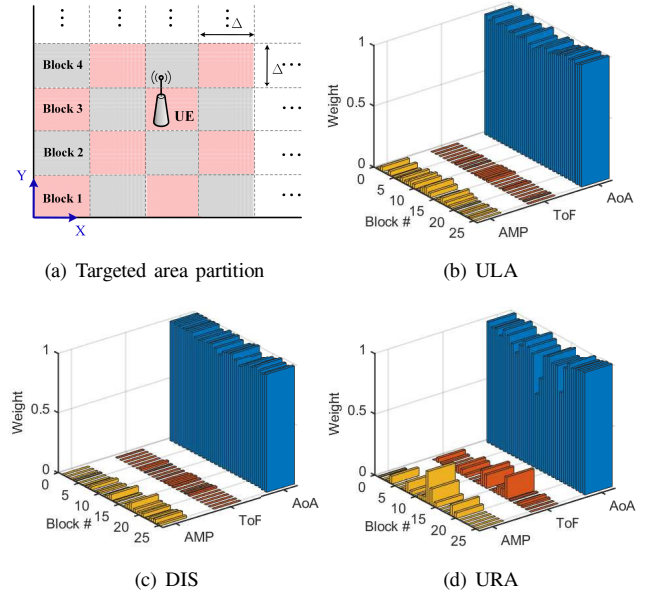


Fig. 7. Weight map construction. (a) Targeted area partition, and  $\Delta$  is the size length of the partition. (b)-(d) Examples of weight assignment for the case of all-metric combination using  $5 \times 5$  blocks. AMP represents the amplitude of MPCs.

(i.i.d.), like [5], [11]. So it is not possible to weight each metric based on a probability density function (PDF) or histogram.

Besides fingerprints map, we also build a weight map for the hybrid-metric classifier [32]. We proposed to partition the targeted area into several blocks built upon the idea of spatial correlation, as presented in Fig. 7(a). In each block, we train a weight vector  $\mathbf{w}_{n_{\text{Block}}} = \{w_{n_{\text{Block}}}^{(i)}\} \in \mathbb{R}^{N_{\text{metric}} \times 1}$  for the hybrid metrics, where  $i$  represents the selected single metric, and  $N_{\text{metric}} = \{1, 2, 3\}$  is the number of metric. Then the weight map for the whole area is given by  $\mathbf{W} = \{\mathbf{w}_{n_{\text{Block}}}\} \in \mathbb{R}^{N_{\text{metric}} \times N_{\text{Block}}}$ ,  $N_{\text{Block}}$  is the number of partition. Based on leave-one-out cross-validation (LOOCV), the weight at  $n_{\text{Block}}$ -th block can be calculated by minimizing the overall positioning errors of each grid (or RPs) in the  $n_{\text{Block}}$ -th block,

$$\begin{aligned} \arg \min_{\mathbf{w}_{n_{\text{Block}}}} \sum_{n_{\text{RP}}} \left\| \mathcal{Y}_{n_{\text{RP}}} - \sum_i \mathcal{M} \left( \mathcal{X}_i | w_{n_{\text{Block}}}^{(i)} \right) \right\|^2, \\ \text{s.t.} \quad \mathbf{w}_{n_{\text{Block}}}^\top \mathbf{1} = 1, \\ w_{n_{\text{Block}}}^{(i)} \in [0, 1], \end{aligned} \quad (14)$$

where  $\mathcal{Y}_{n_{\text{RP}}}$  represents the ground truth of RP in the  $n_{\text{Block}}$ -th block.  $\mathcal{M}(\cdot)$  is the corresponding estimation based on the input metric  $\mathcal{X}$ .  $\mathbf{1}$  denotes a all-ones vector in column form. Equation (14) is a constrained nonlinear optimization problem, which can be solved via quasi-Newton algorithm. It should be noted that the partition on the targeted area should guarantee the problem in (14) to be non-negative definite. In this way, there is one and only one (positive-) definite solution in each block. The calculated weights  $\mathbf{w}_{n_{\text{Block}}}$  of all blocks construct the weight map, which is stored in the local server. For ease of comparison, we have merged the AoA distance (elevation and azimuth) for URA when implementing w-kNN. The adopted angular distance was first introduced to analyze

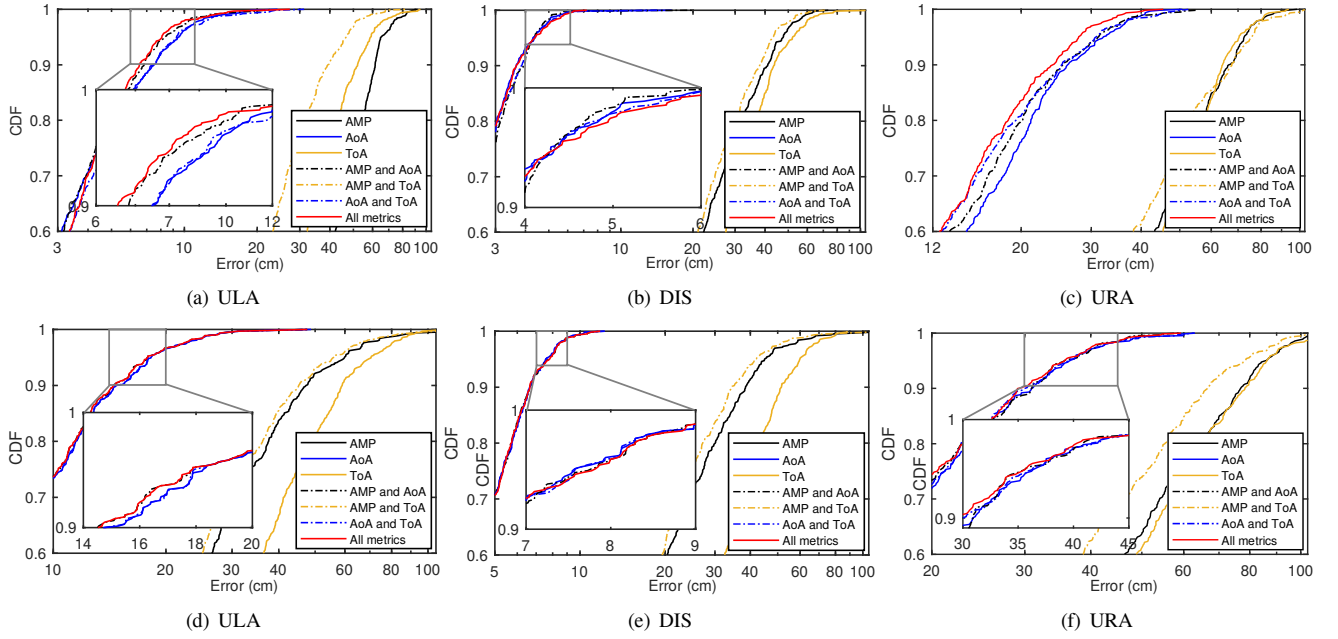


Fig. 8. Positioning accuracy of different single-metric and hybrid-metric schemes based on  $11 \times 11$ -grid fingerprints. (a)-(c) SVR. (d)-(e) w-kNN. AMP represents the amplitude of MPCs.

MPCs' separation in [33]. The merged azimuth and elevation distance of any two AoA measurements is given by,

$$d_{\text{AoA}}^{(i,j)} = \frac{1}{2} \|\Omega_i - \Omega_j\|. \quad (15)$$

where  $\Omega$  is the directional vector defined after (7).

Fig. 7(b)-(d) shows an example of the weight map in case of the all-metric combination. It can be observed that the weights of AoA far exceed the others and approach one. This illustrates that AoA dominates the positioning accuracy in the hybrid-metric scheme. During the online phase, the optimal weights are chosen to average the estimated results of every single metric. A simple method to select the optimal weights from the weight map adopted in this paper is by using the best offline-performing metric as the benchmark. For instance, for the AoA-involved schemes (e.g., AoA-amplitude, AoA-ToF, and all-metric combination), the AoA-based fingerprinting outperforms the other single metrics. Therefore, we select the specific weight block based on the estimation results of AoA.

#### IV. EXPERIMENTAL EVALUATION

##### A. Positioning Performance

In this section, we evaluate the positioning accuracy of the indoor massive MIMO localization system based on the collected CSI dataset. Instead of exploiting CSI directly, we have proposed an MPCs-based fingerprinting system in Section III, which localizes the UE from the perspective of propagation and geometry. Based on the available MPCs, we investigate the positioning accuracy of a single metric (amplitude, AoA, or ToF), as well as the hybrid metrics using the regression and classification model proposed in Section III-B, specifically, SVR and w-kNN. For w-kNN, we choose the four nearest RPs (namely  $k = 4$ ) to weight and obtain the final location. We adopt  $N \times N$ -grid fingerprints for each UE

TABLE I  
PERCENTILE ERRORS OF SVR AND W-KNN IN THE CASE OF  $11 \times 11$ -GRID FINGERPRINTS

Errors (cm)	SVR			w-kNN		
	ULA	DIS	URA	ULA	DIS	URA
Median	2.67	<b>1.88</b>	9.93	6.04	<b>3.93</b>	13.14
90th	6.51	<b>3.65</b>	23.94	14.37	<b>6.64</b>	28.38
95th	7.95	<b>4.38</b>	27.89	17.76	<b>7.77</b>	35.74

to train the model and the residual measurement to evaluate the positioning performance. Fig. 8 presents the cumulative distribution function (CDF) of the positioning errors in the case of  $N = 11$ , namely the resolution of grid is 12.5 cm. Regarding the three single-metric schemes (amplitude, AoA, and ToF), the AoA-based fingerprinting method outperforms the other two metrics distinctly achieving about one-tenth of the positioning errors of ToF- (or amplitude-) based metric. This phenomenon is also consistent with the conclusion in the weight map design. Therefore, when involving AoA in the hybrid-metric schemes, AoA dominates the overall positioning accuracy. Comparing the AoA and all-metric based performance, as shown in Fig. 8, ToF and amplitude only have slight improvement on ULA and URA topologies (about 0.5-2 cm). For the DIS topology, compared to AoA-based accuracy, the all-metric case has no improvement but a little overfitting with 1-2 mm worsening. However, when it comes to the hybrid amplitude-ToF scheme, the accuracy improves distinctly (about 2-10-cm median errors) compared with the single metric (amplitude or ToF).

We summarize the percentile errors of all-metric schemes in Fig. 8 in Table I. It can be observed that DIS achieves the highest accuracy, especially using the SVR model, which has 1.88-cm median positioning errors and 4.38-cm 95-th

TABLE II  
MEAN ABSOLUTE ERRORS OF TRIANGULATION, SVR, AND W-KNN FOR DIFFERENT SIZES OF TRAINING SET IN CM

Grid size	Grid resolution	Triangulation			SVR			w-kNN		
		ULA	DIS	URA	ULA	DIS	URA	ULA	DIS	URA
$6 \times 6$	25.00	8.06	7.57	18.71	5.78	<b>2.50</b>	16.06	14.80	<b>7.49</b>	18.72
$11 \times 11$	12.50				3.48	<b>2.05</b>	13.95	7.69	<b>4.07</b>	15.65
$26 \times 26$	5.00				2.52	<b>1.74</b>	9.97	4.28	<b>2.63</b>	12.55
$51 \times 51$	2.50				1.74	<b>1.63</b>	9.16	1.92	<b>1.91</b>	10.53

percentile errors. Followed by URA with 9.93-cm median errors, ULA achieves the second-highest median errors (2.67-cm) based on SVR. This phenomenon can be explained by the spatial-resolution difference of large-scale antenna array. The distributed array (DIS) is implemented surrounding the targeted area. Therefore, the angular information of all directions can obtain, whereas URA provides the smallest aperture, as well as angular resolution, among the three topologies. When it comes to the regression and classification model, according to Table I, SVR outperforms w-kNN with about 2.05-3.21 cm median errors and 3.39-9.81 cm 95th percentile errors.

Table II further evaluates the impact of antenna topology and fingerprinting algorithm by comparing the MAEs of the all-metric scheme with different sizes of fingerprints, namely  $6 \times 6$ ,  $11 \times 11$ ,  $26 \times 26$ , and  $51 \times 51$ . We also include the positioning errors from triangulation as the AoA is the most accurately estimated MPCs. As shown in Table II, the positioning accuracy of the proposed fingerprinting methods outperforms triangulation generally. But when the grid size is relatively small (e.g.,  $6 \times 6$ -grid), the accuracy of the w-kNN in cases of ULA (14.80-cm MAEs) and URA (18.72-cm MAEs) is worse than the triangulation with MAEs 8.06 cm and 18.71 cm, respectively. For the fingerprinting methods, the accuracy improves with the training set increase, especially for the w-kNN model. The URA has the most significant positioning errors among the three antenna topologies because of the worst spatial resolution among the three topologies. However, it can obtain a distinct accuracy improvement when increasing the size of the training set. The MAEs descend to 10.53 cm and 9.16 cm based on the w-kNN and SVR model, respectively. Meanwhile, we observe that the training set's size has a slight impact on SVR-based ULA and DIS topology. Even though trained with sparse grids (e.g.,  $6 \times 6$ ), ULA and DIS still achieve 5.78-cm and 2.5-cm MAEs, respectively.

Moreover, we also investigate the regression and classification model in the matter of time complexity. For each inference time recording, we repeat the prediction 100 times and obtain the mean values. The operating computer is with Intel(R) Core(TM) i7-7700CPU@3.60GHz and 16 GB RAM. Fig. 9 presents the average inference time of SVR and w-kNN model in the matter of only AoA-based and all-metric schemes. As we can observe, the inference time of the regression model (SVR) fluctuates less (0.4 ms to 1 ms), whereas the computing time for the classifier (w-kNN) increases when more training set adding. This is because the w-kNN will conduct distance calculation with each RP, and the time consumed will increase exponentially despite rapidly reducing errors at the same time. Regarding the antenna topology, the URA has the largest

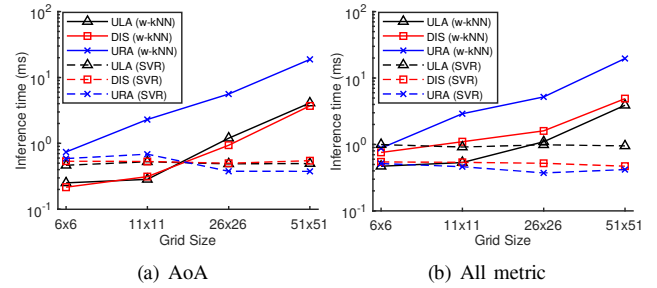


Fig. 9. Inference time of SVR and w-kNN for the single metric and hybrid metrics.

inference time because of the additional matrix calculations that have been introduced when merging the angular distance in (15). Compared with the AoA-based scheme, the inference time of the all-metric scheme has also increased due to more distance metric calculation and higher-dimension feature mapping for w-kNN and SVR, respectively. Overall, when taking accuracy, inference time and system payload (no fingerprint storage required for regression) into account, SVR outperforms w-kNN on the whole in our cases.

## B. Discussion and Future Works

We have proposed the MPCs-based indoor fingerprinting method for a massive MIMO system, which localizes the UE from the perspective of propagation and geometry. Compared with the CNN-based method in [21] using the CSI matrix directly, MPCs-based fingerprinting is generally adaptable to different scenarios and achieves a comparative positioning accuracy. Especially, the DIS topology achieves better accuracy with MAEs 1.63-2.5 cm compared with 8.23-cm MAEs in [21]. However, the accuracy of URA (with MAEs 9.16-16.06 cm) is worse than the CNN-based method, which achieved 5.54-cm MAEs. The reason is two-fold. First, the CNN-based model has utilized much more extensive training sets (tens of thousand samples) than our method (144 to 10404 samples). Second, feeding CSI directly to CNN [21] may learn more knowledge of multipath even though it is a black box. In this paper, we consider the direct link only and neglect the geometrical features from the reflection or scattering due to the strong LoS-scenario in our experiment. By considering those as well, multipath also helps to enhance spatial resolution. Based on the MPCs extracted from the FD-SAGE algorithm, we also can learn the geometry information of reflections and scattering links. The preliminary results in this paper paves the way for the future multipath-assisted localization research in more complex indoor scenarios. Moreover, the consumed



time of training and predicting in the proposed method is much shorter than the CNN-based method [21], because the proposed method reduces the dimension of CSI from  $64 \times 100$  complex matrix to ULA  $57 \times 1$  (or  $57 \times 3$  for hybrid metrics), DIS  $8 \times 1$  (or  $8 \times 3$ ), or URA  $9 \times 1$  (or  $9 \times 3$ ) real matrix using FD-SAGE algorithm, which also relieves system payload to some extent.

For the introduced massive MIMO systems, only nanosecond-level accuracy of ToF estimation was available due to the bandwidth limitation (20 MHz). But one nanosecond corresponds to 30-cm distance errors, which is not sufficient for the centimeter-level (even millimeter-level) positioning. The intuitive solution is to have more bandwidth available, which is difficult (except for the millimeter band) due to the spectrum scarcity in the sub-6 GHz band. In [34], a prototype Chronos was proposed to merge the measurement from several separated bands and stitch them together to give the illusion of a wideband radio. In this way, the authors achieved sub-nanosecond ToF accuracy using WiFi cards. Therefore, improving ToF accuracy based on the signal from the available hopping bands is also the potential direction to further enhance the positioning accuracy of the massive MIMO system.

## V. CONCLUSION

In this paper, we present an MPCs-based indoor fingerprinting system based on the CSI measurement of our massive MIMO testbed. The raw CSI has been calibrated across the antenna and frequency domain using nonlinear regression. On top of that, the MPCs have been extracted based on the FD-SAGE algorithm. Exploiting the amplitude, AoA, and ToF from the direct links, we have implemented the indoor massive MIMO fingerprinting system based on both regression (SVR) and classification model (w-kNN). The following results have been achieved.

- 1) We have investigated the positioning performance in the case of single-metric and hybrid-metric schemes. According to experimental validation, the AoA-based metric outperforms the other metrics in the bandwidth-limited massive MIMO system and dominates the positioning accuracy of any AoA-involved hybrid schemes.
- 2) We have achieved centimeter-level positioning errors generally with the relatively small training set. Especially, the SVR-based DIS topology has achieved 2.50-1.63-cm MAEs regarding different sizes of the training set (namely,  $6 \times 6$ -grid to  $51 \times 51$ -grid for each UE).
- 3) As far as the positioning accuracy, inference time, and system payload, the regression model (SVR) outperforms the classification model (w-kNN) in our cases.

For future work, embracing the MPCs from the reflection or scattering to enhance positioning performance will be investigated (e.g., the multipath-rich scenarios). Furthermore, increasing the ToF accuracy based on the available bandwidth is another potential research direction.

## REFERENCES

- [1] F. Gu, X. Hu, M. Ramezani, D. Acharya, K. Khoshelham, S. Valaee, and J. Shang, "Indoor Localization Improved by Spatial Context: A Survey," *ACM Comput. Surv.*, vol. 52, no. 3, Jul 2019.
- [2] I. Dotlic, A. Connell, H. Ma, J. Clancy, and M. McLaughlin, "Angle of arrival estimation using decawave DW1000 integrated circuits," in *2017 14th Workshop on Positioning, Navigation and Communications (WPNC)*, Oct 2017, pp. 1–6.
- [3] M. Kotaru, K. Joshi, D. Bharadia, and S. Katti, "SpotFi: Decimeter Level Localization Using WiFi," in *Proceedings of the 2015 ACM Conference on Special Interest Group on Data Communication (SIGCOMM)*, Aug 2015, p. 269–282.
- [4] B. Hanssens, D. Plets, E. Tanghe, C. Oestges, D. P. Gaillot, M. Liénard, T. Li, H. Steendam, L. Martens, and W. Joseph, "An Indoor Variance-Based Localization Technique Utilizing the UWB Estimation of Geometrical Propagation Parameters," *IEEE Transactions on Antennas and Propagation*, vol. 66, no. 5, pp. 2522–2533, May 2018.
- [5] C. Li, J. Trogh, D. Plets, E. Tanghe, J. Hoebeke, E. D. Poorter, and W. Joseph, "CRLB-based Positioning Performance of Indoor Hybrid AoA/RSS/ToF Localization," in *2019 International Conference on Indoor Positioning and Indoor Navigation (IPIN)*, Sep 2019, pp. 1–6.
- [6] M. Zhu, J. Vieira, Y. Kuang, K. Åström, A. F. Molisch, and F. Tufvesson, "Tracking and positioning using phase information from estimated multi-path components," in *2015 IEEE International Conference on Communication Workshop (ICCW)*, Jun 2015, pp. 712–717.
- [7] X. Li, E. Leitinger, M. Oskarsson, K. Åström, and F. Tufvesson, "Massive MIMO-Based Localization and Mapping Exploiting Phase Information of Multipath Components," *IEEE Transactions on Wireless Communications*, vol. 18, no. 9, pp. 4254–4267, Sep 2019.
- [8] C. Li, E. Tanghe, D. Plets, P. Suanet, J. Hoebeke, E. De Poorter, and W. Joseph, "ReLoc: Hybrid RSSI- and Phase-Based Relative UHF-RFID Tag Localization With COTS Devices," *IEEE Transactions on Instrumentation and Measurement*, vol. 69, no. 10, pp. 8613–8627, Oct 2020.
- [9] D. Halperin, W. Hu, A. Sheth, and D. Wetherall, "Predictable 802.11 Packet Delivery from Wireless Channel Measurements," in *Proceedings of the ACM SIGCOMM 2010 Conference*, Aug 2010, p. 159–170.
- [10] K. Wu, Jiang Xiao, Youwen Yi, Min Gao, and L. M. Ni, "FILA: Fine-grained indoor localization," in *2012 Proceedings IEEE INFOCOM*, March 2012, pp. 2210–2218.
- [11] J. Xiao, K. Wu, Y. Yi, and L. M. Ni, "FIFS: Fine-Grained Indoor Fingerprinting System," in *2012 21st International Conference on Computer Communications and Networks (ICCCN)*, 2012, pp. 1–7.
- [12] S. Sen, B. Radunovic, R. R. Choudhury, and T. Minka, "You Are Facing the Mona Lisa: Spot Localization Using PHY Layer Information," in *Proceedings of the 10th International Conference on Mobile Systems, Applications, and Services*, ser. MobiSys '12, 2012, p. 183–196.
- [13] L. Chen, I. Ahriz, and D. Le Ruyet, "AoA-Aware Probabilistic Indoor Location Fingerprinting Using Channel State Information," *IEEE Internet of Things Journal*, vol. 7, no. 11, pp. 10 868–10 883, Nov 2020.
- [14] X. Wang, L. Gao, and S. Mao, "CSI Phase Fingerprinting for Indoor Localization With a Deep Learning Approach," *IEEE Internet of Things Journal*, vol. 3, no. 6, pp. 1113–1123, Dec 2016.
- [15] Q. Song, S. Guo, X. Liu, and Y. Yang, "CSI Amplitude Fingerprinting-Based NB-IoT Indoor Localization," *IEEE Internet of Things Journal*, vol. 5, no. 3, pp. 1494–1504, Jun 2018.
- [16] A. Hu, T. Lv, H. Gao, Z. Zhang, and S. Yang, "An ESPRIT-Based Approach for 2-D Localization of Incoherently Distributed Sources in Massive MIMO Systems," *IEEE Journal of Selected Topics in Signal Processing*, vol. 8, no. 5, pp. 996–1011, Oct 2014.
- [17] N. Garcia, H. Wymeersch, E. G. Larsson, A. M. Haimovich, and M. Coulon, "Direct Localization for Massive MIMO," *IEEE Transactions on Signal Processing*, vol. 65, no. 10, pp. 2475–2487, May 2017.
- [18] V. Savic and E. G. Larsson, "Fingerprinting-based positioning in distributed massive mimo systems," in *2015 IEEE 82nd Vehicular Technology Conference (VTC2015-Fall)*, Sep 2015, pp. 1–5.
- [19] A. Decurninge, L. G. Ordóñez, P. Ferrand, H. Gaoning, L. Bojje, Z. Wei, and M. Guillaud, "CSI-based Outdoor Localization for Massive MIMO: Experiments with a Learning Approach," in *2018 15th International Symposium on Wireless Communication Systems (ISWCS)*, Aug 2018, pp. 1–6.
- [20] M. Arnold, J. Hoydis, and S. t. Brink, "Novel Massive MIMO Channel Sounding Data applied to Deep Learning-based Indoor Positioning," in *12th International ITG Conference on Systems, Communications and Coding (SCC)*, Feb 2019, pp. 1–6.
- [21] S. D. Bast, A. P. Guevara, and S. Pollin, "CSI-based Positioning in Massive MIMO systems using Convolutional Neural Networks," in *IEEE 91st Vehicular Technology Conference (VTC2020-Spring)*, May 2020, pp. 1–5.

- [22] A. P. Guevara, S. De Bast, and S. Pollin, "Weave and Conquer: A Measurement-based Analysis of Dense Antenna Deployments," *arXiv preprint arXiv:2003.11467*, 2020.
- [23] National Instrument, "5G Massive MIMO Testbed: From Theory to Reality," [Online] <https://www.ni.com/nl-be/innovations/white-papers/14/5g-massive-mimo-testbed--from-theory-to-reality--.html>, Mar 2019.
- [24] S. De Bast and S. Pollin, "Ultra Dense Indoor MaMIMO CSI Dataset," [IEEE Dataport]. Available: <https://dx.doi.org/10.21227/nr6k-8r78>, Feb 2021.
- [25] M. Speth, S. A. Fechtel, G. Fock, and H. Meyr, "Optimum receiver design for wireless broad-band systems using OFDM. I," *IEEE Transactions on Communications*, vol. 47, no. 11, pp. 1668–1677, Nov 1999.
- [26] N. Tadayon, M. T. Rahman, S. Han, S. Valaee, and W. Yu, "Decimeter Ranging With Channel State Information," *IEEE Transactions on Wireless Communications*, vol. 18, no. 7, pp. 3453–3468, Jul 2019.
- [27] A. Tarighat, R. Bagheri, and A. H. Sayed, "Compensation Schemes and Performance Analysis of IQ Imbalances in OFDM Receivers," *IEEE Transactions on Signal Processing*, vol. 53, no. 8, pp. 3257–3268, Aug 2005.
- [28] H. Zhu, Y. Zhuo, Q. Liu, and S. Chang, " $\pi$ -Splicer: Perceiving Accurate CSI Phases with Commodity WiFi Devices," *IEEE Transactions on Mobile Computing*, vol. 17, no. 9, pp. 2155–2165, Sep 2018.
- [29] C. C. Chong, D. I. Laurenson, C. M. Tan, S. McLaughlin, M. A. Beach, and A. R. Nix, "Joint detection-estimation of directional channel parameters using the 2-D frequency domain SAGE algorithm with serial interference cancellation," in *2002 IEEE International Conference on Communications. (ICC2002)*, Apr 2002, pp. 906–910.
- [30] B. H. Fleury, M. Tschudin, R. Heddergott, D. Dahlhaus, and K. Ingeman Pedersen, "Channel parameter estimation in mobile radio environments using the SAGE algorithm," *IEEE Journal on Selected Areas in Communications*, vol. 17, no. 3, pp. 434–450, Mar 1999.
- [31] A. J. Smola and B. Schölkopf, "A Tutorial on Support Vector Regression," *Statistics and computing*, vol. 14, no. 3, pp. 199–222, Aug 2004.
- [32] S. Fang, Y. Hsu, and W. Kuo, "Dynamic Fingerprinting Combination for Improved Mobile Localization," *IEEE Transactions on Wireless Communications*, vol. 10, no. 12, pp. 4018–4022, Dec 2011.
- [33] M. Steinbauer, H. Ozelik, H. Hofstetter, C. F. Mecklenbrauker, and E. Bonek, "How to Quantify Multipath Separation," *IEICE transactions on electronics*, vol. 85, no. 3, pp. 552–557, Mar 2002.
- [34] D. Vasisht, S. Kumar, and D. Katabi, "Sub-Nanosecond Time of Flight on Commercial Wi-Fi Cards," in *Proceedings of the 2015 ACM Conference on Special Interest Group on Data Communication*, ser. SIGCOMM '15, Aug 2015, p. 121–122.